ADVANCED MATERIALS
www.advmat.d

Magnetoactive Acoustic Metamaterials

*Kunhao Yu, Nicholas X. Fang, Guoliang Huang, and Qiming Wang**

Acoustic metamaterials with negative constitutive parameters (modulus and/or mass density) have shown great potential in diverse applications ranging from sonic cloaking, abnormal refraction and superlensing, to noise canceling. In conventional acoustic metamaterials, the negative constitutive parameters are engineered via tailored structures with fixed geometries; therefore, the relationships between constitutive parameters and acoustic frequencies are typically fixed to form a 2D phase space once the structures are fabricated. Here, by means of a model system of magnetoactive lattice structures, stimuli-responsive acoustic metamaterials are demonstrated to be able to extend the 2D phase space to 3D through rapidly and repeatedly switching signs of constitutive parameters with remote magnetic fields. It is shown for the first time that effective modulus can be reversibly switched between positive and negative within controlled frequency regimes through lattice buckling modulated by theoretically predicted magnetic fields. The magnetically triggered negative-modulus and cavity-induced negative density are integrated to achieve flexible switching between single-negative and double-negative. This strategy opens promising avenues for remote, rapid, and reversible modulation of acoustic transportation, refraction, imaging, and focusing in subwavelength regimes.

Artificial materials with tailored geometries and elastic properties to enable smart control of acoustic waves have enjoyed diverse applications ranging from cloaking, abnormal refraction and superlensing, to noise canceling.[1–6] These acoustic metamaterials are different from traditional phononic crystals because they can achieve abnormal control over the frequency regime with the wavelength much larger than their size scales.[7] The underlying mechanism primarily relies on local resonance–induced negative constitutive parameters (e.g., modulus or mass density) that enable abnormal acoustic transmission forbiddance/dissipation within the local resonance–related frequency regime, rather than the frequency regime governed by their size scales.[4–6] Following the essential idea, negative mass density or bulk modulus have been achieved using multiphase composites,[8–11] membrane arrays,[12–14] or Helmholtz resonators,[15,16] respectively; and the double-negative can be achieved via integrating two mechanisms.[17–25] Despite these pioneering studies, the existing studies of negative constitutive parameters usually rely on structures with fixed configurations; and therefore, the relevant frequency regime may not be modulated once the structures are fabricated.[4,5] It is naturally desirable to achieve active control of the acoustic metamaterials over the existence and frequency regime of the negative constitutive parameters to expand their application potential.

Starting from the seminal works done by Lakes and co-workers,[26–28] the active control of negative structural stiffness has been achieved through mechanical force–induced elastic instabilities.[29–31] This instability associated negative structural stiffness has been demonstrated to lead to significantly enhanced mechanical loss factors[29–31] and thus improved energy dissipation of the structures.[32–39] More recently, this mechanical force–enabled active control of negative stiffness has also been employed to dissipate acoustic waves within acoustic metamaterials.[40,41] Compared to direct mechanical loadings, remote physical stimuli[42–44] are more appealing because of their special advantages including noncontact with the structures, nonlocal modulation, and rapid switching. However, using remote physical stimuli to modulate the sign of effective constitutive parameters of acoustic metamaterials remains unexplored.

Compared to the traditional control of constitutive parameters whose signs only depend on the acoustic frequency, the remote stimuli add another dimension of control to form a 3D phase space of the constitutive parameters (**Figure 1**). To prove the concept, we here present a strategy of using remote magnetic fields to reversibly deform lattice structures to enable on-demand switching effective constitutive parameter pairs among double-positive, single-negative, and double-negative (Figure 1). We first harness the magnetically triggered structural buckling of elastomer lattices to achieve controlled negative-modulus within designed acoustic frequency regimes. Then, integrating the magnetically triggered negative modulus and the cavity-induced negative density, we demonstrate reversible switching between single-negative and double-negative. Theories are developed to

K. Yu, Prof. Q. Wang
Sonny Astani Department of Civil and Environmental Engineering
University of Southern California
Los Angeles, CA 90089, USA
E-mail: qimingw@usc.edu
Prof. N. X. Fang
Department of Mechanical Engineering
Massachusetts Institute of Technology
Cambridge, MA 02139, USA
Prof. G. Huang
Department of Mechanical and Aerospace Engineering
University of Missouri
Columbia, MO 65211, USA

DOI: 10.1002/adma.201706348

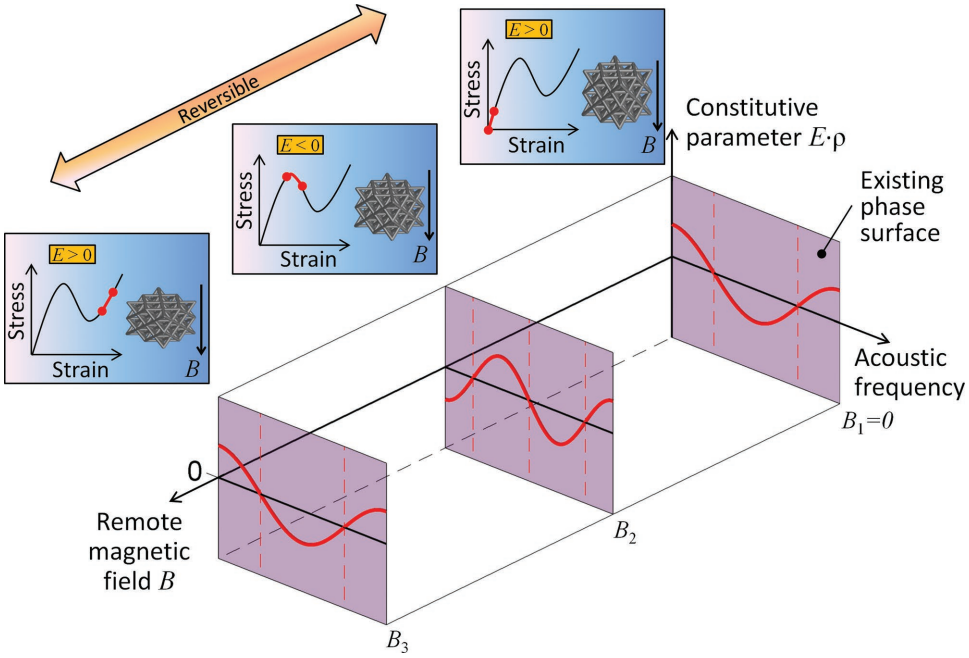

Figure 1. Conceptual idea of the study. We harness the magnetically induced lattice buckling to enable tunable sign of effective modulus E between positive and negative. This principle can be applied to lattice structures with designed negative mass density ρ to enable versatile switching of constitutive pairs (E and ρ) among double-positive, single-negative, and double-negative. The switching is reversible and remote.

understand the magnetic control of the metalattices and corresponding negative constitutive parameters. We expect that this strategy may potentially open promising avenues for stimuli-responsive acoustic metamaterials to achieve remote, rapid, and reversible modulation of the acoustic transportation, refraction, imaging, and focusing in low-frequency regimes.

To enable magnetically actuated structural buckling, we employ a lattice structure, octet truss, which sustains magnetic field–induced compressive loadings primarily through axial compressive forces (**Figure 2**a). The structure would undergo buckling when the axial forces reach a threshold. We use a ferromagnetic particle–reinforced elastomer as the constituent material and fabricate the lattice structure through the stereolithography-based manufacturing method (Figure 2a,b).[45,46] Then, we fix the lattice structure on the bottom and apply a controlled magnetic field B through the lattice (Figure S1, Supporting Information). As the magnetic field ramps up, the lattice deforms and folds its beams to reduce its height while maintaining the lateral dimensions (Figure 2c and Movie S1, Supporting Information). Initially, the lattice smoothly decreases its height, and then suddenly becomes unstable at a magnetic field $B_{1c} = 0.24$ T, dramatically reducing its height via buckling a structural layer (Figure 2ci–iii). As the magnetic field further ramps up, the lattice first decreases its height smoothly and then undergoes another structural buckling at a magnetic field $B_{2c} = 0.36$ T (Figure 2civ–vi). Further ramping up the magnetic field squeezes the lattice beams until the lattice structure is fully compacted. To quantify the lattice deformation, we calculate the effective strain of the lattice as $\varepsilon = 1 - H/H_0$, where H_0 and H are heights of the undeformed and deformed lattice, respectively. We plot the relationship between the lattice strain ε and the applied magnetic field B in Figure 2d. The curve shows two consecutive jumps at magnetic fields B_{1c} and B_{2c}. The magnetically actuated lattice folding is reversible and can be very rapid. As the magnetic field decreases, the folded lattice can reversibly unfold and return to its initial geometry and height (Figure 2cvii). As we apply cyclic magnetic fields through the lattice with a period of 4 s, the lattice can deform accordingly with a high resilience (Figure 2e and Movie S2, Supporting Information).

It is noted that the magnetically induced lattice buckling stems from the stretching-dominated nature of the octet truss.[47,48] This architecture obeys the Maxwell criterion so that the architecture is self-constrained to enable the loading to be primarily carried via the axial compressive forces (Figure 2a).[47–49] Similar magnetically induced buckling may not be observed for bending-dominated lattice structures.[45,47,48]

Then, we demonstrate that the magnetically triggered buckling can be harnessed to enable controlled negative modulus within designed frequency regimes. We first apply a magnetic field to the lattice structure, and then measure the incremental stress $\Delta\sigma$ when an incremental compressive displacement perturbation Δd is applied (**Figure 3**a,b and Figure S2, Supporting Information). When the magnetic field is small ($B_1 = 0.12$ T), the incremental displacement can induce monotonically increasing positive incremental stress (Figure 3ai). When the magnetic field ($B_2 = 0.23$ T) is close to the buckling magnetic field B_{1c}, the incremental stress first increases slightly and then decreases monotonically to negative (Figure 3aii). Similar negative incremental stress can be observed for the magnetic field ($B_4 = 0.35$ T) close to buckling magnetic field B_{2c} (Figure 3aiv); however, the incremental stresses are always positive for other magnetic field regimes (Figure 3aiii,v). We further calculate the effective modulus of the magnetically folded lattice as $E = \Delta\sigma H_0/\Delta d$, and

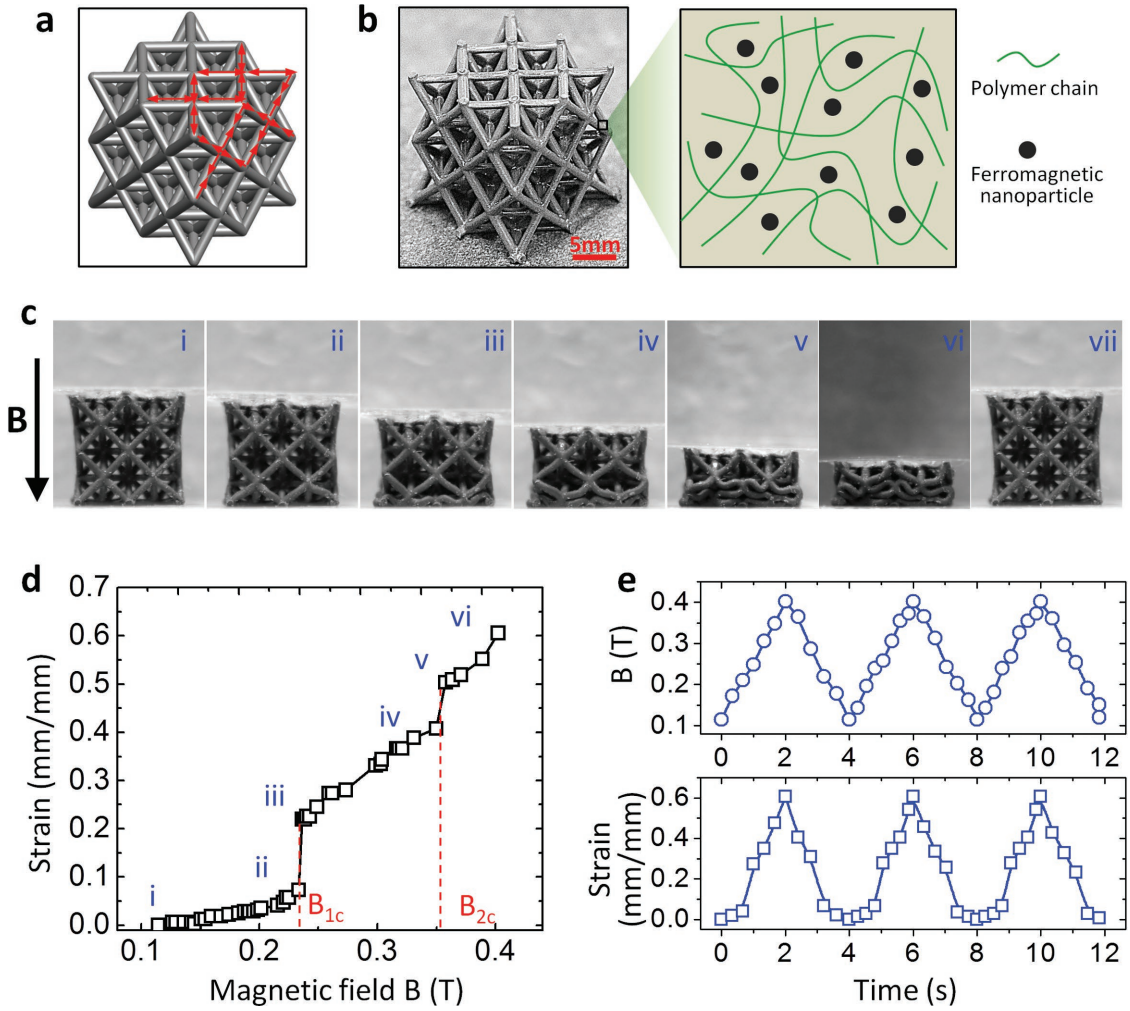

Figure 2. Magnetoactuation of the elastomer lattice. a) Schematic of the octet-truss lattice. The red arrows illustrate the loadings along the beam. b) Fabricated magnetoactive lattice structure comprising of elastomers and ferromagnetic nanoparticles. c) Image sequence of the lattice structure under increasing magnetic fields. (vii) Image of the lattice when the magnetic field retreats. d) The effective strain of the lattice as a function of the magnetic field B. e) The effective lattice strain as the applied magnetic field periodically oscillates.

then plot as functions of the incremental displacement (Figure 3b). The modulus E is always positive for the lattice under magnetic fields B_1, B_3, and B_5, but decreases from positive to negative for B_2 and B_4 which are close to two buckling magnetic fields, respectively. Under magnetic fields B_2 and B_4, the lattice shows negative modulus when the applied incremental displacement is larger than $\Delta d_2^* \approx \Delta d_4^* \approx 0.045$ mm, respectively (Figure 3bii–iv). It is noted that the negative stiffness is measured when the lattice structure is under constraints: the lattice is constrained on the bottom platform, then subjected to a magnetic field, and finally constrained on the top by a loading plate (Figure S2, Supporting Information).

The negative incremental modulus can be qualitatively understood as follows. As the magnetic field is close to but less than the buckling magnetic field, the lattice is deformed close to the buckling state. A small incremental compressive displacement can trigger the lattice buckling, after which the reaction force of the lattice becomes negative. On the other hand, if the applied magnetic field is larger or much smaller than the buckling magnetic fields, incremental displacement cannot trigger lattice buckling, and thus can only induce positive modulus. Therefore, only left side of the buckling magnetic field can trigger negative modulus if a sufficiently large incremental displacement is applied ($\Delta d > \Delta d_2^*$ at B_2 and $\Delta d > \Delta d_4^*$ at B_4).

Next, we harness the negative modulus to control acoustic waves. In conducting an acoustic wave, we consider the lattice structure as an effective medium where the material particles are activated to move back and forth to transfer the acoustic energy. The material displacement amplitude δ can be roughly estimated as[50,51]

$$\delta \approx \frac{\sqrt{W/A}}{\sqrt[4]{E\rho/\left[3(1-2\nu)\right]2\pi f}} \tag{1}$$

where W is the acoustic power, A is the cross-section area, f is the regular acoustic frequency, ρ is the effective mass

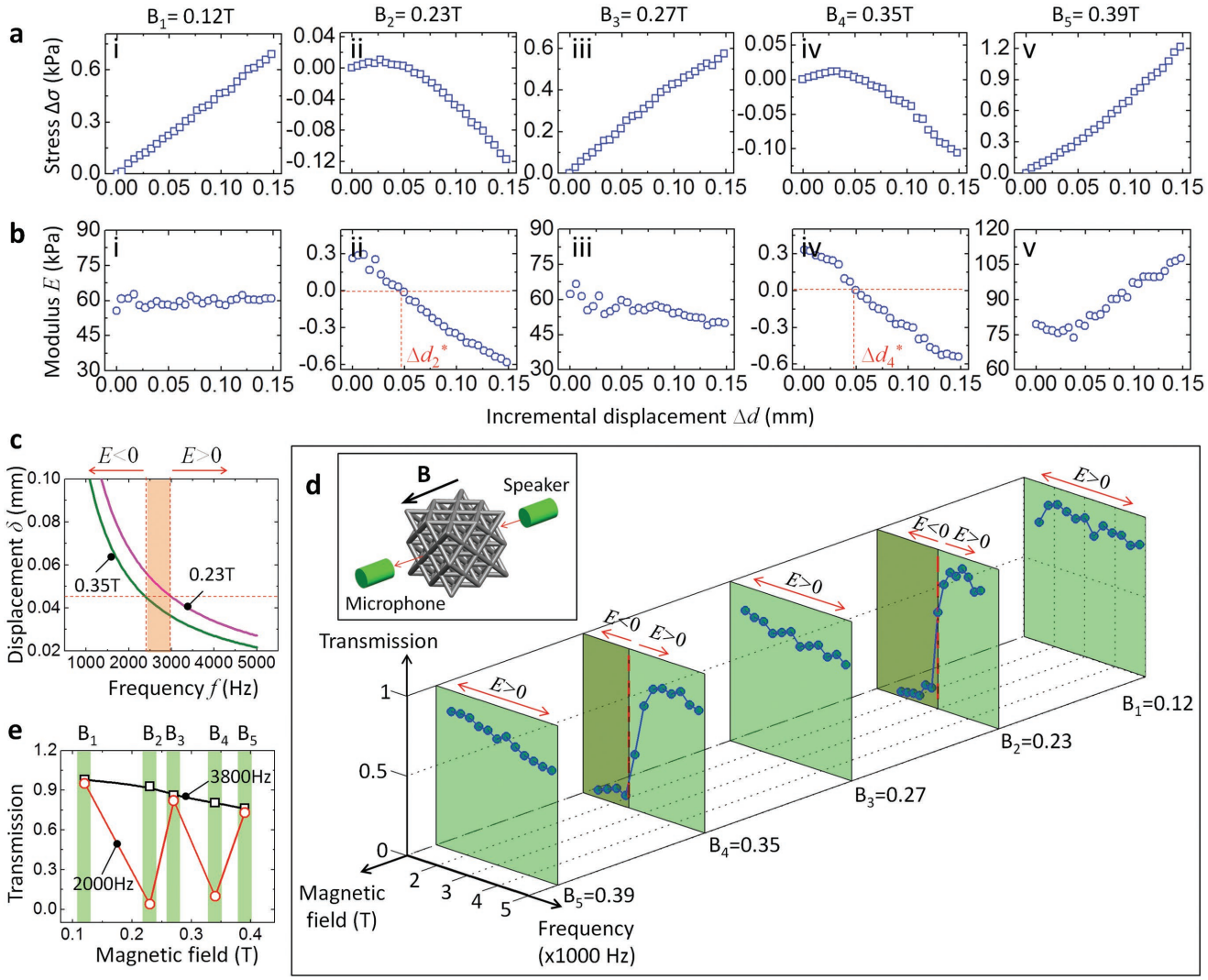

Figure 3. Switching modulus between positive and negative with magnetic fields. a,b) Incremental stresses and moduli of the lattice under various magnetic fields as functions of incremental displacements Δd. c) Material displacement amplitudes under magnetic fields 0.23 and 0.35 T as functions of acoustic frequencies. d) The measured acoustic transmissions of the lattice under various magnetic fields. The inset illustrates the schematic for the experimental system. e) The acoustic transmission of the lattice under various magnetic fields and acoustic frequencies 2000 and 3800 Hz, respectively.

density, E is the effective Young's modulus, and ν is the effective Poison's ratio. As we estimate the effective modulus as the modulus with $\Delta d = 0$ in Figure 2bii,iv, we can obtain the lower-bound of the material displacement amplitude which is a monotonically decreasing function of the acoustic frequency f (Figure 3c). When the material displacement amplitude δ is larger than Δd_2^* or Δd_4^*, the lattice can be considered to be deformed by a displacement with sufficient amplitude to reach the negative-modulus regimes. Correspondingly at the magnetic field B_2, the effective modulus of the lattice is considered as negative for $f < 3000$ Hz and positive for $f > 3000$ Hz (Figure 3c). Similarly, at the magnetic field B_4, the threshold frequency is 2400 Hz (Figure 3c).

To verify the negative modulus, we measure the acoustic transmission through the magnetically deformed lattice structure (experimental setup shown in the inset of Figure 3d and Figure S3, Supporting Information). The acoustic propagation direction is aligned with the magnetic field direction. The lattice is first constrained on the bottom, then subjected to a magnetic field, and finally exposed to the incoming acoustic wave along the magnetic field direction (Figure S3, Supporting Information). When an acoustic metamaterial has negative modulus and positive density, the acoustic wave will be significantly dissipated within the lattice, and the system thus shows a low acoustic transmission.[4,5] We here measure the acoustic transmission of the magnetically deformed lattice structure within a large range of frequency from 1000 to 5000 Hz (inset of Figure 3d). We find that under magnetic fields B_1, B_3, and B_5 the acoustic transmissions are all relatively high (>0.75) over 1000–5000 Hz (Figure 3d, simulation verification in Figure S4a,b, Supporting Information). However, under magnetic fields B_2 and B_4, the acoustic transmissions become relatively

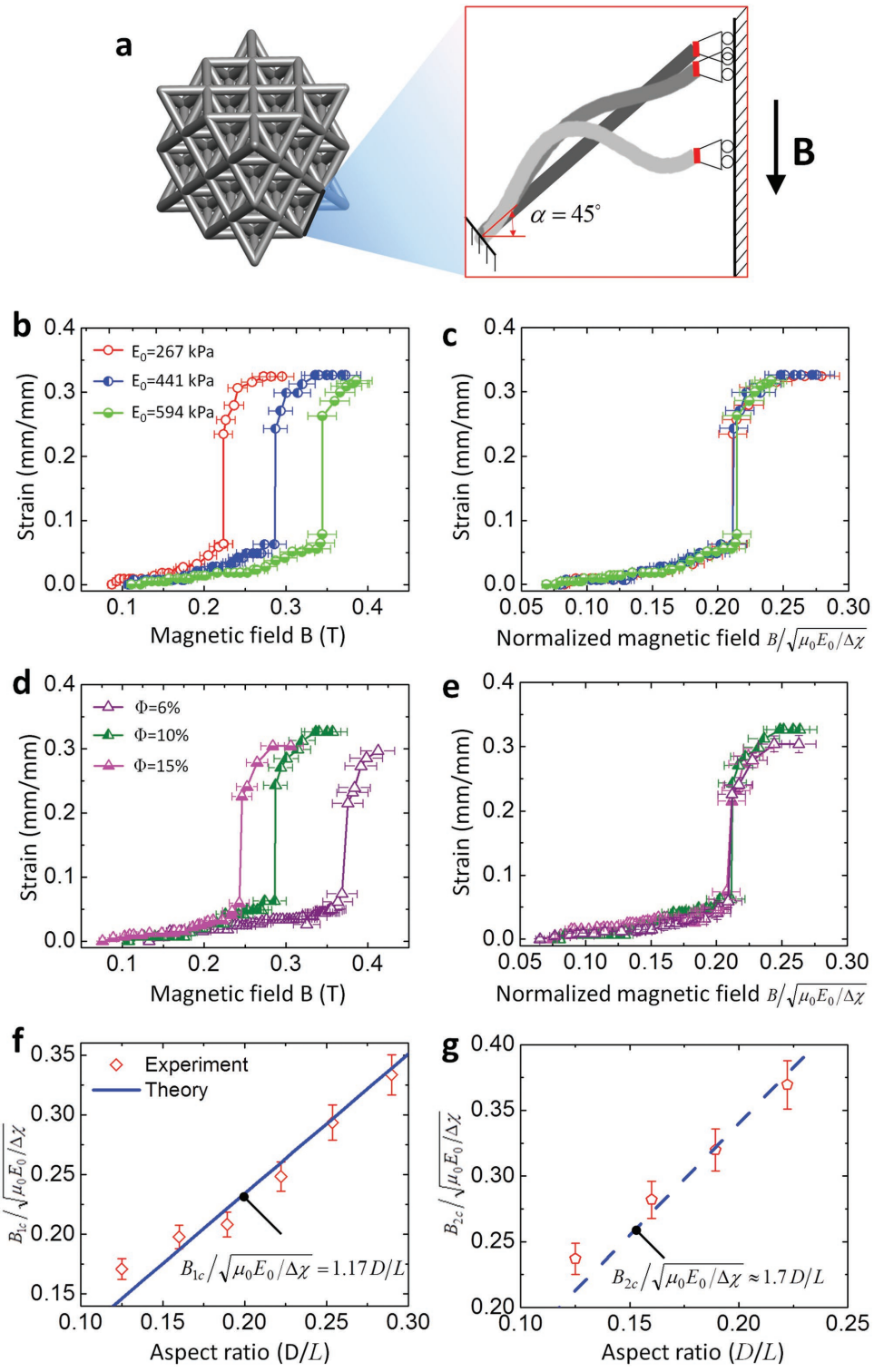

Figure 4. Understanding of the magnetically induced deformation. a) Schematic of the representative tilted beam within the octet lattice. b,c) Effective strains of the lattices with varied elastomer moduli in functions of magnetic fields and normalized magnetic fields, respectively. d,e) Effective strains of the lattices with various volume fractions of ferromagnetic nanoparticles in functions of magnetic fields and normalized magnetic fields, respectively. f) Critical normalized magnetic fields of the first buckling as a function of beam aspect ratios. g) Critical normalized magnetic fields of the second buckling as a function of beam aspect ratios.

low (<0.15) below 3000 and 2700 Hz, respectively. The observed threshold frequencies for the low-acoustic-transmissions roughly agree with the predicted threshold frequencies related to the negative moduli at B_2 and B_4 (Figure 3c,d). From another perspective, the magnetic field can enable flexible switching of the modulus sign over the low-frequency regime (<3000 Hz,

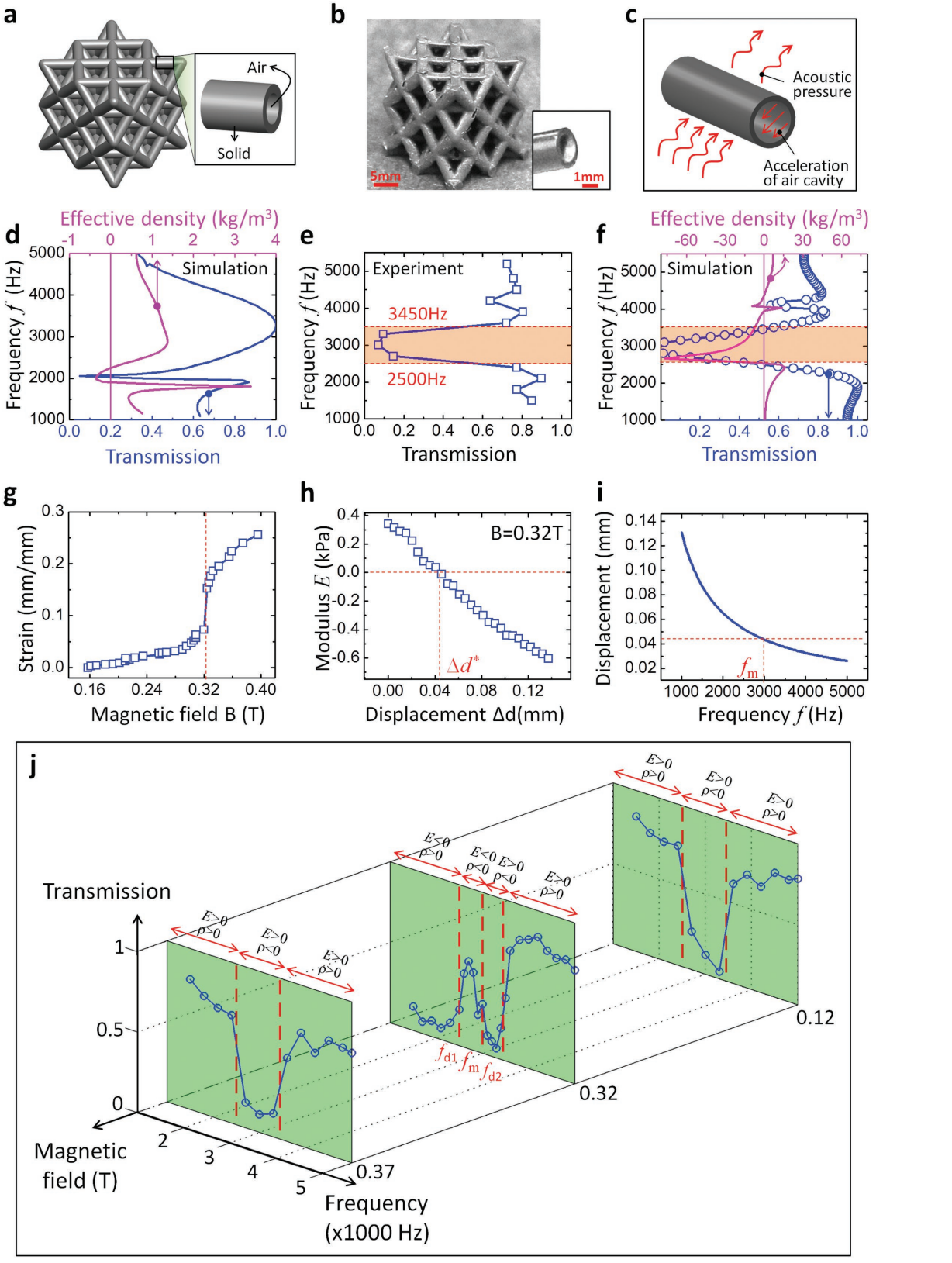

Figure 5. Switching between single-negative and double-negative with magnetic fields. a) Schematic for the hollow octet-truss lattice. b) Fabricated hollow octet-truss lattice. c) Schematic to show the acceleration of the air medium within the hollow cavity around the acoustic resonance. d) Numerically simulated acoustic transmission through an elastomer tube and corresponding effective density as functions of acoustic frequencies. e) Experimentally measured acoustic transmissions of the lattice as a function of acoustic frequencies. f) Computationally calculated acoustic transmission and

Figure 3e). For example, at 2000 Hz, the acoustic transmission is 0.95 under B_1, and then sequentially changes to 0.04 under B_2, 0.82 under B_3, 0.1 under B_4, and 0.74 under B_5. However, at 3800 Hz, the acoustic transmissions under various magnetic fields B_1–B_5 remain above 0.75.

It is noted that the acoustic-triggered negative stiffness of the magnetically deformed lattice is relatively special for the remote magnetic actuation. Previous works on materials and structures with constrained elastic instability usually do not exhibit overall negative stiffness, because the instability is usually constrained by direct mechanical means, e.g., surrounding elastic medium or direct mechanical compression.[26–31,41] However, we here employ the remote magnetic field that is fundamentally different from the direct mechanical means. Under the remote magnetic fields, the top surface of the lattice is still relatively free. The second load coming from a loading plate or an acoustic wave can still induce incremental displacement of the material/structure. That is why we still can capture the negative stiffness through an incremental plate loading (Figure 3a,b) or an incoming acoustic wave (Figure 3d).

To verify the experimental results, we flip the acoustic transportation direction and measure the acoustic transmission of the lattice under various magnetic fields (Figure S5, Supporting Information). The results are very similar to those shown in Figure 3d, demonstrating the reciprocal character of the system. To further verify the experimental results, we measure the threshold frequency of the low-acoustic-transmission for varied acoustic powers W (0.1–0.25 w) (Figure S6, Supporting Information). According to Equation (1), the threshold frequency should follow $f_c \propto \sqrt{W}$. The measured threshold frequencies roughly agree with this scaling law (Figure S6, Supporting Information).

The versatile control of the modulus sign requires quantitative control of the magnetically induced lattice deformation. To quantitatively understand the magnetically controlled lattice deformation, we first focus the deformation of a representative tilted beam within the periodic lattice (**Figure 4**a). The free energy of the magnetic field–deformed tilted beam can be written as (derivation in Supporting Information)[52–56]

$$\Pi = \int_0^L \frac{\pi E_0 D^4}{128}\left(\frac{\mathrm{d}\theta}{\mathrm{d}s}\right)^2 \mathrm{d}s - \int_0^L \frac{\pi D^2}{4}\left[\int_0^{\mathbf{B}} \mathbf{M}\cdot \mathrm{d}\mathbf{B}\right]\mathrm{d}s \tag{2}$$

where s is the curvilinear coordinate along the beam, θ is the angle between the tangent line and the horizontal axis, E_0 is Young's modulus of the magnetoactive elastomer, L is the beam length, D is the beam diameter, $\mathbf{B}$ is the applied magnetic field vector, and $\mathbf{M}$ is magnetization vector. The variation of Equation (2) leads to a governing equation written as

$$\lambda^2\left(\frac{\mathrm{d}^2\theta}{\mathrm{d}s^2}\right) + \sin(2\theta + 2\alpha) = 0 \tag{3}$$

where $\lambda = \sqrt{E_0\mu_0 D^2/(8B^2\Delta\chi)}$ is a characteristic length, $\mu_0 = 4\pi \times 10^{-7} N \cdot A^{-2}$ is the magnetic permittivity of the vacuum, and α is the initial tilted angle of the beam. $\Delta\chi$ is the effective magnetic susceptibility difference between the axial and orthogonal direction and can be estimated as $\Delta\chi \approx \chi - \chi/(1+\chi/2)$, where χ is the magnetic susceptibility of the elastomer (derivation in Supporting Information).

At the critical point of the buckling, the characteristic length λ should scale with the beam length L. Therefore, the critical magnetic field of the first buckling should follow a scaling law as

$$B_{1C} \propto \frac{D}{L}\sqrt{\frac{\mu_0 E_0}{\Delta\chi}} \tag{4}$$

where D is the beam diameter. As shown in Equation (4), the critical magnetic field is governed by the elastomer modulus E_0, magnetic sensitivity $\Delta\chi$, and beam aspect ratio D/L.

To validate the scaling law in Equation (4), we first fabricate lattice structures using elastomers with different moduli via changing the crosslink density (Figure S7a,b, Supporting Information) and measure the lattice strain in a function of the applied magnetic field (Figure 4b). The modulus of the elastomer markedly affects the critical magnetic field of the first buckling (Figure 4b). When the applied magnetic field is normalized with $\sqrt{\mu_0 E_0/\Delta\chi}$, the curves for different moduli coincide (Figure 4c). Then, we vary the concentration of the ferromagnetic particles within the elastomers, which affects both the modulus and the magnetic susceptibility (Figure S7c,d, Supporting Information). The ferromagnetic particle concentration can also remarkably affect the critical magnetic field of the first buckling (Figure 4d); however, these curves coincide again after normalizing the magnetic field with $\sqrt{\mu_0 E_0/\Delta\chi}$ (Figure 4e). Moreover, we carry out the magnetoactuation experiments on lattice structures with various beam aspect ratios (Figure S8, Supporting Information), and find that the normalized magnetic field $B/\sqrt{\mu_0 E_0/\Delta\chi}$ is approximately in a linear relation with the beam aspect ratios, which is consistent with the scaling law shown in Equation (4) (Figure 4f).

To further elucidate the coefficient of the scaling law in Equation (4), we theoretically calculate the critical magnetic field of the first buckling (details in Figure S9 in the Supporting Information). We employ the magnetoelastica model under an assumption that the elastomer beam is inextensible along the axial direction.[57] The theoretically calculated critical magnetic field $B_{1C} \approx 1.17(d/L)\sqrt{\mu_0 E_0/\Delta\chi}$ roughly agrees with the experimental results with small discrepancies (Figure 4f). The discrepancies primarily stem from the inextensibility assumption that may not be fully obeyed by the experimental samples.

We further plot the normalized critical magnetic fields of the second structural buckling in a function of beam aspect ratios (Figure 4g). We find that the magnetic fields of the second buckling also follow the similar scaling law as Equation (4), with the coefficient as 1.7.

effective density of the lattice as functions of acoustic frequencies. g) The effective strain of the hollow octet lattice as a function of the applied magnetic field. h) Incremental modulus of the lattice under the magnetic field 0.32 T as a function of incremental displacements. i) The material displacement amplitude of the lattice as a function of acoustic frequencies. j) The acoustic transmission of the hollow octet lattice under magnetic fields 0.12, 0.32, and 0.37 T as functions of acoustic frequencies.

Next, we use the magnetic fields to enable switching between single-negative and double-negative (negative modulus and negative mass density). To design a structure with a negative mass density within certain frequency regimes, we acquire inspirations from existing studies on air-separated membrane arrays that exhibit negative effective mass densities,[12,13,18,22,58,59] and fabricate a hollow elastomer lattice with sealed air cavities (**Figure 5**a,b).[45,46] Around the antiresonance frequency, the air medium within the hollow cavity moves out of phase with the incident wave, inducing the effective acceleration direction different from the incoming acoustic pressure (Figure 5c). According to the effective medium theory, the effective mass density of the excited elastomer tube with the air cavity can be estimated as[8,15,58,60]

$$\rho = \rho_0 \left(1 - \frac{G f_1^2}{f^2 - f_1^2 + i\Gamma f/2\pi} \right) \tag{5}$$

where ρ_0 is the air mass density, f_1 is the air resonance frequency, G is the geometrical factor, and Γ is the dissipation loss in the air cavity. When the frequency is close to the resonance frequency, the real part of the effective mass density becomes negative. Numerical simulations of the acoustic transportation through a single elastomer tube show that the effective density becomes negative around 2000 Hz (Figure 5d). Therefore, the acoustic transmission becomes significantly low within a narrow frequency band that is roughly corresponding to the frequency band for the negative mass density (Figure 5d and Figure S4c,d, Supporting Information).

When a number of elastomer tubes are connected to form a hollow lattice, the low-transmission band is expected to be further expanded. To determine the low-transmission frequency band (f_{d1}, f_{d2}) of the hollow lattice, we measure the acoustic transmission through the stress-free lattice within frequency 1000–5000 Hz (Figure 5e). The transmission within 2500 Hz < f < 3450 Hz is dramatically smaller than those in other frequency regimes. Therefore, we determine frequency regime for the negative density as (f_{d1} = 2500, f_{d2} = 3450) Hz. To verify the experimental results, we carry out numerical simulations which show that the simulated frequency regimes of the low-transmission and the negative density can roughly match the experimental results (Figure 5e,f and Figure S4e,f, Supporting Information).

To enable the magnetically controlled structural folding, we apply controlled magnetic fields through the hollow lattice (Figure 5g). With increasing magnetic fields, the lattice undergoes a structural buckling right after the magnetic field 0.32 T. The structure can only exhibit one structural buckling within 0.42 T that is the limit magnetic field of our experimental setup. Further incremental perturbation tests show that the magnetically deformed lattice (B = 0.32 T) shows negative modulus when the acoustic frequency is smaller than $f_m \approx$ 3000 Hz (Figure 5h,i).

Combining the negative modulus and mass density, we can flexibly switch between single-negative and double-negative using the magnetic fields (Figure 5j). When the applied magnetic field is 0.12 and 0.37 T, the lattice structure is mechanically stable with positive modulus. Therefore, the acoustic transmission only shows a low-transmission band from 2500 to 3450 Hz associated with the negative density (Figure 5j). However, when the applied magnetic field is around 0.32 T, the density is negative within (2500, 3450) Hz and the modulus is negative for the frequency below 3000 Hz. Accordingly, the frequency is separated into four regimes with different constitutive parameter pairs (Figure 5j): $\rho > 0$ and $E < 0$ for (1000, 2500) Hz, $\rho < 0$ and $E < 0$ for (2500, 3000) Hz, $\rho < 0$ and $E > 0$ for (3000, 3450) Hz, and $\rho > 0$ and $E > 0$ for (3450, 5000) Hz. The acoustic transmission for the single-negative regime is relatively low, i.e., below 0.15 within (1000, 2500) and (3000, 3450) Hz. However, the acoustic transmission for double-positive and double-negative is relatively high, i.e., above 0.75 within (3450, 5000) Hz and reaching 0.6 within (2500, 3000) Hz.[17–23] Similar multiphase behaviors have been realized in composite acoustic metamaterials with simultaneously negative modulus and mass density.[18] The current work demonstrates another dimension of flexibility: the double-negative can be reversibly switched on and off using the applied magnetic fields (Figure 5j). Specifically, from 0.12 to 0.37 T, single-negative can be tuned to double-negative, and then back to single-negative within frequency regime (2500, 3450) Hz.

To justify that the observed stop-band (2500, 3450) Hz is not related to Bragg effect or waveguide effect that is lattice size–dependent, we argue from two aspects: 1) The transmission shows a stop-band within (2500, 3450) Hz for low B (0.12 T), and then returns to the similar stop band at the higher B (0.37 T) with much higher filling fraction and smaller size scale. This shows that the lattice size may not play a role in determining the stop-band. 2) Additionally, we carry out finite-element simulations on hollow lattices with the deformed geometries but very high material stiffness (Figure S10, Supporting Information). We find that the bandgap does not exist for these rigid lattices. These simulations imply that only geometry is insufficient to generate the observed stop-band behaviors in Figure 5j.

Moreover, we turn on and off the negative stiffness through tuning the acoustic power to validate that the multiphase behavior shown in Figure 5j at B = 0.32 T is indeed a double-negative phenomenon. According to Figure S6 (Supporting Information), the threshold frequency f_c for the modulus sign change should be a function of acoustic power W as $f_c \propto \sqrt{W}$. In Figure 5j, we employ acoustic power $W \approx$ 0.25 w, and we observe the multiphase behavior at B = 0.32 T. However, if we employ a lower acoustic power $W \approx$ 0.033 w, we cannot observe the similar multiphase behavior at B = 0.32 T, but only one bandgap associated with negative density (Figure S11, Supporting Information). It is because the threshold frequency for the modulus sign change is lower than 1000 Hz.

In summary, we introduce a paradigm of using remote magnetic fields to reversibly switch constitutive parameters of acoustic metamaterials among double-positive, single-negative, and double-negative. As a model system for stimuli-responsive acoustic metamaterials that can modulate the sign of effective modulus using low magnetic fields (<0.4 T), the system may be easily translated to acoustic switch devices that can tune on and off the acoustic transportation with various remote stimuli.[42,43] In addition, this system with the capability of switching on and off double-negative constitutive parameters offers a promising opportunity for acoustic devices with indices switching between

positive and negative, and these devices may be potentially used for switchable acoustic refraction, imaging, and focusing.[17–23] Furthermore, as a model system harnessing abnormal stress–strain behaviors associated with the mechanical instability,[61] the current method constructs a unique tunnel that bridges the quasi-static structural response and the dynamic wave transportation.[40,62,63]

Experimental Section

Sample Preparation: The magnetoactive lattice structures were fabricated using the stereolithography-based manufacturing method (method reported elsewhere[45,46]). Briefly, water-soluble hollow lattice structures were first manufactured using the projection stereolithography, and then the magnetoactive elastomers were cured within the hollow channels, followed by the dissolution of the scaffold, leaving the elastomer lattice structures.[45] The water-soluble photoresin is a mixture of *N*,*N*-dimethylacrylamide, methacrylic acid and methacrylic anhydride, polyvinylpyrrolidone, and photoinitiator phenylbis(2,4,6-trimethylbenzoyl)phosphine oxide. Silicone elastomers Mold max NV14 (with crosslinking agent versus base 0.06–0.14 by weight, Smooth-on, USA) mixed with iron nanoparticles (0.03–0.16 by volume, Sigma-Aldrich, USA) were employed as the elastomer presolutions. The elastomers were cured at 25 °C for 12 h. The dissolution of the hollow lattices was carried out in a NaOH solution (1 mol L^{-1}) for 6 h.

Observation of Lattice Deformation: Figure S1 (Supporting Information) illustrated the experimental setup for in situ observation of the deformation of the lattice structures under magnetic fields. The lattice structures were first bonded to a thin plate (1 mm). A permanent magnet Neodymium Ring N45 (CMS magnets, USA) or a computer-controlled metal-core solenoid 14B35 (The science source, USA) was placed on the bottom of the plate to apply a magnetic field to the lattice structure. The magnetic field was measured with a Gaussmeter (Model GM1-ST, EMR Shielding Solutions). The magnetic fields from the permanent magnet and the solenoid were modulated by controlling the distance between the magnet and the lattices (Figure S1, Supporting Information) and the current through the solenoid, respectively. The magnetic field around the middle height of the lattice was denoted as the applied magnetic field. To ensure homogeneous height reduction under magnetic fields, the lattice was capped by a thin glass slide (100 μm) whose weight could be negligible. The lattice strain was calculated as $\varepsilon = 1 - H/H_0$, where H and H_0 are the heights of the undeformed and deformed lattice, respectively. The lattice heights were calculated by averaging over four positions of the lattice.

Measurement of the Incremental Modulus: Figure S2 (Supporting Information) illustrated the experimental setup for the measurement of the incremental modulus of the magnetically deformed lattice. Bottom-fixed lattices were first deformed with a magnetic field and then mounted on an Instron mechanical tester (Instron 5942). The top loading plate then applied a small displacement on the lattice structure. The top loading plate was protected by plastics to eliminate the interaction with the magnetic fields.

Measurement of Acoustic Transmission: A cap was first 3D-printed using a Markerbot to leave a center hole to place the lattice structure. The cap was then assembled onto one end of a plastic tube (diameter 5 cm, McMaster Carr, USA). A magnet ring was placed close to the lattice structure to apply a magnetic field. A function generator (PI-8127, PASCO, USA) controlled loudspeaker (OT19NC00-04, Tymphany) was placed in the plastic tube to provide the acoustic signal. The acoustic power was controlled by the applied electric current on the speaker. The acoustic signal was collected by a microphone (378B02 with 426E01, PCB Piezotronics, USA) placed in the magnet ring, and processed by a signal conditional (482C05, PCB Piezotronics) and displaced by an oscilloscope (TBS1052B, Tektronix, USA). To reduce the acoustic reflection within the plastic tube, cotton pads were attached to the inner wall of the tube to absorb the acoustic signals. The acoustic transmission was measured as $|P_w/P_{wo}|$, where P_w and P_{wo} are microphone-measured acoustic pressure with and without the lattice structure, respectively.[63]

Acoustic Simulation: Numerical simulations were implemented with the acoustic module in COMSOL Multiphysics v5.2—a commercial finite element software. Figure S4a,c,e (Supporting Information) illustrated the numerical set-ups for the simulations. Two phases elastomer solid and air were involved in the numerical models. For the lattice solid, density 1100 kg m^{-3} was employed and sound speed was estimated based on the elastomer modulus (Figure S7, Supporting Information). Considering the periodicity of the lattice structures, symmetric boundary condition was applied in the lateral direction. Perfectly matching layers were employed to ensure the open boundary along the acoustic transport direction. The simulation was validated by benchmark calculations and the mesh accuracy was ascertained through a mesh refinement study.

Supporting Information

Supporting Information is available from the Wiley Online Library or from the author.

Acknowledgements

Q.W. and K.Y. acknowledge the funding support from National Science Foundation (CMMI-1649093) and from Air Force Office of Scientific Research Young Investigator Program with Program Manager Dr. Jaimie S. Tiley. G.H. acknowledges the support from the Air Force Office of Scientific Research under Grant No. AF 9550-15-1-0016 with Program Manager Dr. Byung-Lip (Les) Lee.

Conflict of Interest

The authors declare no conflict of interest.

Keywords

acoustic metamaterials, double negative, magnetoactive materials, negative index

Received: November 1, 2017
Revised: January 25, 2018
Published online:

[1] S. Zhang, C. Xia, N. Fang, *Phys. Rev. Lett.* **2011**, *106*, 024301.
[2] S. Zhang, L. Yin, N. Fang, *Phys. Rev. Lett.* **2009**, *102*, 194301.
[3] N. Kaina, F. Lemoult, M. Fink, G. Lerosey, *Nature* **2015**, *525*, 77.
[4] G. Ma, P. Sheng, *Sci. Adv.* **2016**, *2*, e1501595.
[5] S. A. Cummer, J. Christensen, A. Alù, *Nat. Rev. Mater.* **2016**, *1*, 16001.
[6] M. Yang, P. Sheng, *Annu. Rev. Mater. Res.* **2017**, *47*, 83.
[7] R. Martinezsala, J. Sancho, J. V. Sánchez, V. Gómez, J. Llinares, F. Meseguer, *Nature* **1995**, *378*, 241.
[8] Z. Liu, X. Zhang, Y. Mao, Y. Zhu, Z. Yang, C. T. Chan, P. Sheng, *Science* **2000**, *289*, 1734.
[9] Y. Lai, Y. Wu, P. Sheng, Z.-Q. Zhang, *Nat. Mater.* **2011**, *10*, 620.
[10] G. Ma, C. Fu, G. Wang, P. del Hougne, J. Christensen, Y. Lai, P. Sheng, *Nat. Commun.* **2016**, *7*, 13536.
[11] Y. Chen, G. Hu, G. Huang, *J. Mech. Phys. Solids* **2017**, *105*, 179.
[12] S. H. Lee, C. M. Park, Y. M. Seo, Z. G. Wang, C. K. Kim, *Phys. Rev. A* **2009**, *373*, 4464.

[13] G. Ma, M. Yang, S. Xiao, Z. Yang, P. Sheng, *Nat. Mater.* **2014**, *13*, 873.
[14] Z. Yang, J. Mei, M. Yang, N. Chan, P. Sheng, *Phys. Rev. Lett.* **2008**, *101*, 204301.
[15] N. Fang, D. Xi, J. Xu, M. Ambati, W. Srituravanich, C. Sun, X. Zhang, *Nat. Mater.* **2006**, *5*, 452.
[16] S. H. Lee, C. M. Park, Y. M. Seo, Z. G. Wang, C. K. Kim, *J. Phys.: Condens. Matter* **2009**, *21*, 175704.
[17] J. Li, C. Chan, *Phys. Rev. E* **2004**, *70*, 055602.
[18] S. H. Lee, C. M. Park, Y. M. Seo, Z. G. Wang, C. K. Kim, *Phys. Rev. Lett.* **2010**, *104*, 054301.
[19] Y. Ding, Z. Liu, C. Qiu, J. Shi, *Phys. Rev. Lett.* **2007**, *99*, 093904.
[20] T. Brunet, A. Merlin, B. Mascaro, K. Zimny, J. Leng, O. Poncelet, C. Aristégui, O. Mondain-Monval, *Nat. Mater.* **2015**, *14*, 384.
[21] M. Yang, G. Ma, Z. Yang, P. Sheng, *Phys. Rev. Lett.* **2013**, *110*, 134301.
[22] Y. Wu, Y. Lai, Z.-Q. Zhang, *Phys. Rev. Lett.* **2011**, *107*, 105506.
[23] Y. Xie, B.-I. Popa, L. Zigoneanu, S. A. Cummer, *Phys. Rev. Lett.* **2013**, *110*, 175501.
[24] X. Liu, G. Hu, G. Huang, C. Sun, *Appl. Phys. Lett.* **2011**, *98*, 251907.
[25] R. Zhu, X. Liu, G. Hu, C. Sun, G. Huang, *Nat. Commun.* **2014**, *5*, 5510.
[26] R. Lakes, *Philos. Mag. Lett.* **2001**, *81*, 95.
[27] R. S. Lakes, T. Lee, A. Bersie, Y. Wang, *Nature* **2001**, *410*, 565.
[28] R. Lakes, *Phys. Rev. Lett.* **2001**, *86*, 2897.
[29] D. Kochmann, W. Drugan, *Proc. R. Soc. A* **2012**, rspa20110546.
[30] C. S. Wojnar, D. M. Kochmann, *Philos. Mag.* **2014**, *94*, 532.
[31] T. Klatt, M. R. Haberman, *J. Appl. Phys.* **2013**, *114*, 033503.
[32] T. Frenzel, C. Findeisen, M. Kadic, P. Gumbsch, M. Wegener, *Adv. Mater.* **2016**, *28*, 5865.
[33] B. Haghpanah, L. Salari-Sharif, P. Pourrajab, J. Hopkins, L. Valdevit, *Adv. Mater.* **2016**, *28*, 7915.
[34] D. M. Correa, C. C. Seepersad, M. R. Haberman, *Integr. Mater. Manuf. Innovation* **2015**, *4*, 1.
[35] S. Shan, S. H. Kang, J. R. Raney, P. Wang, L. Fang, F. Candido, J. A. Lewis, K. Bertoldi, *Adv. Mater.* **2015**, *27*, 4296.
[36] K. Che, C. Yuan, J. Wu, H. J. Qi, J. Meaud, *J. Appl. Mech.* **2017**, *84*, 011004.
[37] A. Rafsanjani, A. Akbarzadeh, D. Pasini, *Adv. Mater.* **2015**, *27*, 5931.
[38] D. Restrepo, N. D. Mankame, P. D. Zavattieri, *Extreme Mech. Lett.* **2015**, *4*, 52.
[39] M. E. Pontecorvo, S. Barbarino, G. J. Murray, F. S. Gandhi, *J. Intell. Mater. Syst. Struct.* **2013**, *24*, 274.
[40] P. Wang, F. Casadei, S. Shan, J. C. Weaver, K. Bertoldi, *Phys. Rev. Lett.* **2014**, *113*, 014301.
[41] N. Nadkarni, C. Daraio, D. M. Kochmann, *Phys. Rev. E* **2014**, *90*, 023204.
[42] B.-I. Popa, S. A. Cummer, *Nat. Commun.* **2014**, *5*, 3398.
[43] S. Xiao, G. Ma, Y. Li, Z. Yang, P. Sheng, *Appl. Phys. Lett.* **2015**, *106*, 091904.
[44] M. Lapine, I. V. Shadrivov, D. A. Powell, Y. S. Kivshar, *Nat. Mater.* **2012**, *11*, 30.
[45] Y. Jiang, Q. Wang, *Sci. Rep.* **2016**, *6*, 34147.
[46] T. Li, Y. Jiang, K. Yu, Q. Wang, *Soft Matter* **2017**, *13*, 7731.
[47] V. Deshpande, M. Ashby, N. Fleck, *Acta Mater.* **2001**, *49*, 1035.
[48] L. J. Gibson, M. F. Ashby, *Cellular Solids: Structure and Properties*, Cambridge University Press, Cambridge **1999**.
[49] J. Maxwell, *Philos. Mag.* **1864**, *27*, 294.
[50] M. Bruneau, *Fundamentals of Acoustics*, John Wiley & Sons, NY, **2013**.
[51] L. Brillouin, *Wave Propagation in Periodic Structures: Electric Filters and Crystal Lattices*, Courier Corporation, MA **2003**.
[52] P. Yih-Hsing, Y. Chau-Shioung, *Int. J. Eng. Sci.* **1973**, *11*, 415.
[53] L. D. Landau, E. M. Lífshíts, L. Pitaevskii, *Electrodynamics of Continuous Media*, Vol. *8*, Pergamon Press, Oxford **1984**.
[54] S. V. Kankanala, N. Triantafyllidis, *J. Mech. Phys. Solids* **2004**, *52*, 2869.
[55] F. C. Moon, Y.-H. Pao, *J. Appl. Mech.* **1968**, *35*, 53.
[56] F. Gerbal, Y. Wang, F. Lyonnet, J.-C. Bacri, T. Hocquet, M. Devaud, *Proc. Natl. Acad. Sci. USA* **2015**, *112*, 7135.
[57] S. Timoshenko, *Theory of Elastic Stability*, Tata McGraw-Hill Education, NY **1970**.
[58] H. Chen, H. Zeng, C. Ding, C. Luo, X. Zhao, *J. Appl. Phys.* **2013**, *113*, 104902.
[59] C. M. Park, J. J. Park, S. H. Lee, Y. M. Seo, C. K. Kim, S. H. Lee, *Phys. Rev. Lett.* **2011**, *107*, 194301.
[60] S. H. Lee, O. B. Wright, *Phys. Rev. B* **2016**, *93*, 024302.
[61] Z. Nicolaou, A. Motter, *Nat. Mater.* **2012**, *11*, 608.
[62] K. Bertoldi, *Annu. Rev. Mater. Res.* **2017**, *47*, 51.
[63] S. Babaee, N. Viard, P. Wang, N. X. Fang, K. Bertoldi, *Adv. Mater.* **2015**, *28*, 1631.